Chemical Engineering Journal 444 (2022) 136449

Contents lists available at ScienceDirect

Chemical Engineering Journal

journal homepage: www.elsevier.com/locate/cej

Room temperature gas sensors based on Ce doped TiO_2 nanocrystals for highly sensitive NH_3 detection

Kaidi Wu [a,b], Marc Debliquy [b], Chao Zhang [a,*]

[a] College of Mechanical Engineering, Yangzhou University, Yangzhou 225127, PR China
[b] Service de Science des Matériaux, Fault Polytechnique, Université de Mons, Mons 7000, Belgium

ARTICLE INFO

Keywords:
Ce doped TiO_2
Gas sensor
Ammonia
Room temperature
DFT

ABSTRACT

Room-temperature gas sensors with high performance have shown unexpected potential in practical application. This work developed a series of Ce doped TiO_2 nanocrystals via microwave-assisted solvothermal method for detecting ammonia (NH_3) at room temperature. All the samples presented small-size nanocrystals and good crystallinity. The 0.43 at% Ce-TiO_2 nanocrystals with a large specific surface area of 266.9 $m^2 \cdot g^{-1}$ exhibited the distinguished NH_3 sensing performance at room temperature, including high response (23.99 @ 20 ppm), low limit of detection (140 ppb), superior selectivity, repeatability, and operating stability. The enhanced sensing mechanisms were explained by the synergetic strategy of re-orientated high energy facets, oxygen vacancy and large specific surface area, which boost the surface activity and charge transfer efficiency. The enhanced sensing mechanism was further verified through DFT calculations. Moreover, the practical application potential was also evaluated for the fish freshness detection. This work will provide a direction that rapidly synthesizing rare earth element doped metal oxides for high-performance room temperature gas sensors.

1. Introduction

Ammonia is a kind of toxic gas with a strong irritating smell, which can stimulate the skin and respiratory system. As one of the atmospheric and indoor pollutants, it will present a grave threat to human health once people are exposed to low concentration NH_3 for a long time [1]. In addition, NH_3 is also a biomarker gas for meat freshness assessment (including fish and poultry), which is released via microorganisms and endogenous enzymes decomposing sulfhydryl-containing amino acids and proteins during the spoilage process [2]. The concentration of released NH_3 will reach or even exceed ppm level if the meat starts spoiling [3]. Furthermore, the variation of trace-amounts NH_3 in human exhaled breath is recommended as a biomarker for diagnosing some diseases [4]. Hence, it is critically urgent to develop low-cost and high-performance gas sensors for NH_3 monitoring.

Metal oxides-based chemi-resistive gas sensors with the advantage of easy-integrated and high sensitivity have attracted a wide range of attention, which is a possible technique to realize real-time detection [5]. However, it still face the challenge of low recovery speed and insufficient detection range. Several methods have been developed to overcome the limitation, such as designing unique nanostructures, modifying the surface state of sensing layers through loading noble metals, doping with metal elements and constructing homo/hetero-junction via compounding with second component [6–9]. Among these strategies, doping with rare earth elements presents the potential in attaining better gas sensing properties. Zhao et al. studied the solvothermal synthesized ZnO nanowires doped with Ce, Eu, and Er gas sensors, it is concluded that approximate doping content contributes to improving the ethanol sensing properties at 300 °C [10]. Ma et al. investigated the Pr-doped In_2O_3 nanoparticles synthesized via a solvothermal route. They found Pr doping contributes to enhancing ethanol sensing properties at 240 °C [11]. Wang et al. reported Ce doped α-Fe_2O_3 sensors presented enhanced sensing response towards acetone at 220 °C [12]. Though the improvement in gas sensing performance is attained, the high operating temperature remains, which has several main drawbacks, including high power consumption and poor reproducibility, limiting its practical application.

Ultra-small size nanocrystals with unique size and surface properties are expected for wide applications, such as energy storage, catalysis, and room temperature sensor [13]. As for room temperature chemi-resistance based gas sensing, maximizing the available surface area and charge transport properties play the crucial role in attaining high

* Corresponding author at: College of Mechanical Engineering, Yangzhou University, Huayang West Road 196, Yangzhou 225127, Jiangsu Province, PR China.
E-mail address: zhangc@yzu.edu.cn (C. Zhang).

https://doi.org/10.1016/j.cej.2022.136449
Received 17 February 2022; Received in revised form 20 March 2022; Accepted 14 April 2022
Available online 19 April 2022

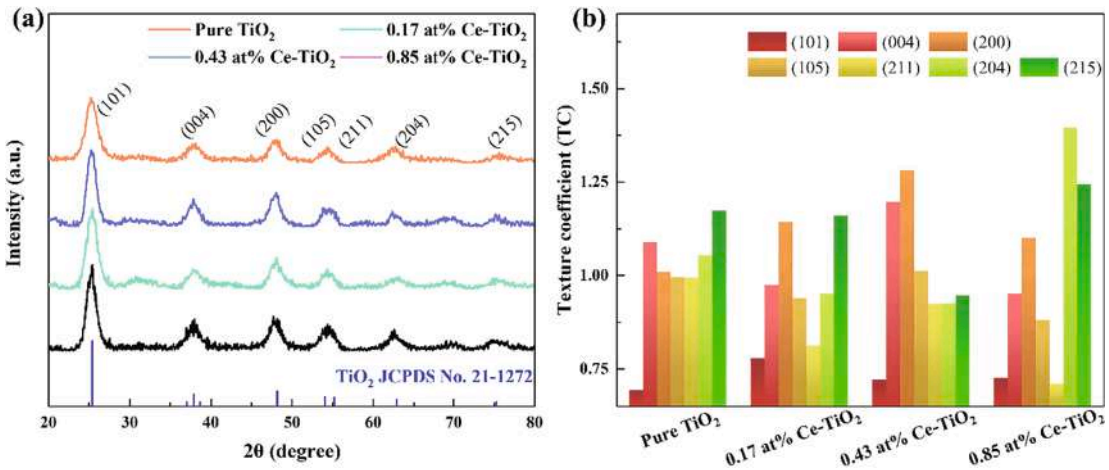

Fig. 1. (a) XRD patterns of as-synthesized TiO_2 and Ce-TiO_2 samples and (b) texture coefficient values of the samples.

performance [14]. Hence, in view of receptor function and utilization efficiency, the ultra-small size nanocrystals may be a promised candidate for room temperature gas sensing.

To our best knowledge, there is limit research about rare earth elements doped metal oxides small-size nanocrystals for room temperature gas sensors in previous literature. Herein, we utilized a synergetic strategy to develop Ce doped TiO_2 nanocrystals based NH_3 sensor working at room temperature, which is still limited research at present. These samples were solvothermal synthesized rapidly under microwave field heating. The effect of minute-quantity Ce doping on nanostructure was investigated using necessary characterization methods and the room temperature NH_3 sensing properties were also studied. The surface conduction model analysis and density functional theory study were conducted to explain the enhanced sensing mechanism. Furthermore, we also explored the application in fish (Pangasius) freshness detection to confirm its practicality. This facile and efficient strategy will contribute to prospering room-temperature gas sensors for practical applications.

2. Experimental section

2.1. Synthesis of TiO_2 and Ce-TiO_2 nanocrystals

Ce-TiO_2 nanocrystals were synthesized via as following procedures: 30 mL absolute ethanol and 3 mL nitric acid aqueous solution (3 M) was mixed in a beaker and stirred for 30 min. Subsequently, 10 mL tetrabutyl titanate (TBT) and $Ce(NO_3)_3{\cdot}6H_2O$ were dissolved into the above solution slowly. After magnetically stirring for 1.5 h, it was transferred to a 60 mL Teflon lined autoclave and kept into the microwave-assisted synthesis instrument (XH-800G, Beijing Xianghu Technologies Development Co., Ltd.) at 120 °C and 500 W for 1 h. The synthesized precipitates were washed and centrifuged with absolute ethanol for 4 times, eventually dried at 70 °C for 12 h. Pure TiO_2 was synthesized using the same procedure without $Ce(NO_3)_3{\cdot}6H_2O$. The four samples were then dissolved in ethanol, which is denoted as pure TiO_2, 0.17 at% Ce-TiO_2, 0.43 at% Ce-TiO_2 and 0.85 at% Ce-TiO_2.

2.2. Characterization

The crystal structure of four samples were identified using X-ray diffraction with Cu-Kα radiation (XRD, D8 Advance Bruker). The nanostructure was determined via transmission electron microscopy (TEM, JEM-2100), and a further analysis was conducted using high-resolution transmission electron microscopy (HRTEM, Tecnai G2 F30 S-TWIN). X-ray photoelectron spectroscopy (XPS, Thermo Fisher Scientific ESCALAB 250Xi) was used to analyze surface chemical compositions. The specific surface area was calculated through N_2 adsorption/desorption isotherms at 77 K (Autosorb IQ3, Quantachrome Instruments). The surface oxygen vacancies were further verified through electron paramagnetic resonance (EPR, A300-10/12, Bruker).

2.3. Fabrication and measurement of gas sensors

The obtained powders were directly used to obtain their slurry with deionized water, subsequently coated onto the sensor substrate. The gas sensor was obtained after dried and treated at 120 °C for 24 h. As shown in Fig. S1, the room temperature (25 ± 2 °C) gas sensor testing system (Wuhan Huachuang Ruike Technology Co., Ltd.) can show the real-time electrical resistance signals. The more test details can be found in Supplementary data. The n-type response is defined as R_a/R_g, where R_a is the stable sensor resistance in air and R_g is the stable sensor resistance in target gas. The response/recovery time is the time taken for achieving 90% change of resistance in the response and recovery behaviors.

The fish spoilage detection is explored through the homemade measurement equipment (Fig. S2). The defrosted fillet (fresh Pangasius, 25 g) was placed in a 0.6 L sealed bottle at room temperature. The total gas flow was set as 500 sccm. The ambient air and the spoilage gas were successively injected into the chamber using pumps to detect fish spoilage state. The variation of electrical resistance at different storage stages (1, 6, 12, 18 and 24 h) were recorded, and the corresponding released NH_3 concentrations were calculated to assess the fish freshness.

2.4. DFT calculation details

The simulated adsorption behavior between target gas and sensing material surface was studied by the CASTEP modules of Material Studio software. The details can be found in Supplementary data. The adsorption energy of NH_3 molecules on (0 0 1) TiO_2/Ce-TiO_2 was calculated using Eq. (1):

$$E_{ads} = E_{total} - \left(E_{(001)} + E_{NH3}\right) \quad (1)$$

where E_{total} is the total energy of the NH_3 molecules-(0 0 1) TiO_2/Ce-TiO_2 surface system, $E_{(0\ 0\ 1)}$ is the energy of (0 0 1) TiO_2/Ce-TiO_2 surface, and E_{NH3} is the energy of the isolated NH_3 molecule.

3. Results and discussion

3.1. Characterization results

Fig. 1a shows the phase compositions of as-synthesized powders and standard diffraction patterns of anatase TiO_2 (JCPDS No. 21–1272).

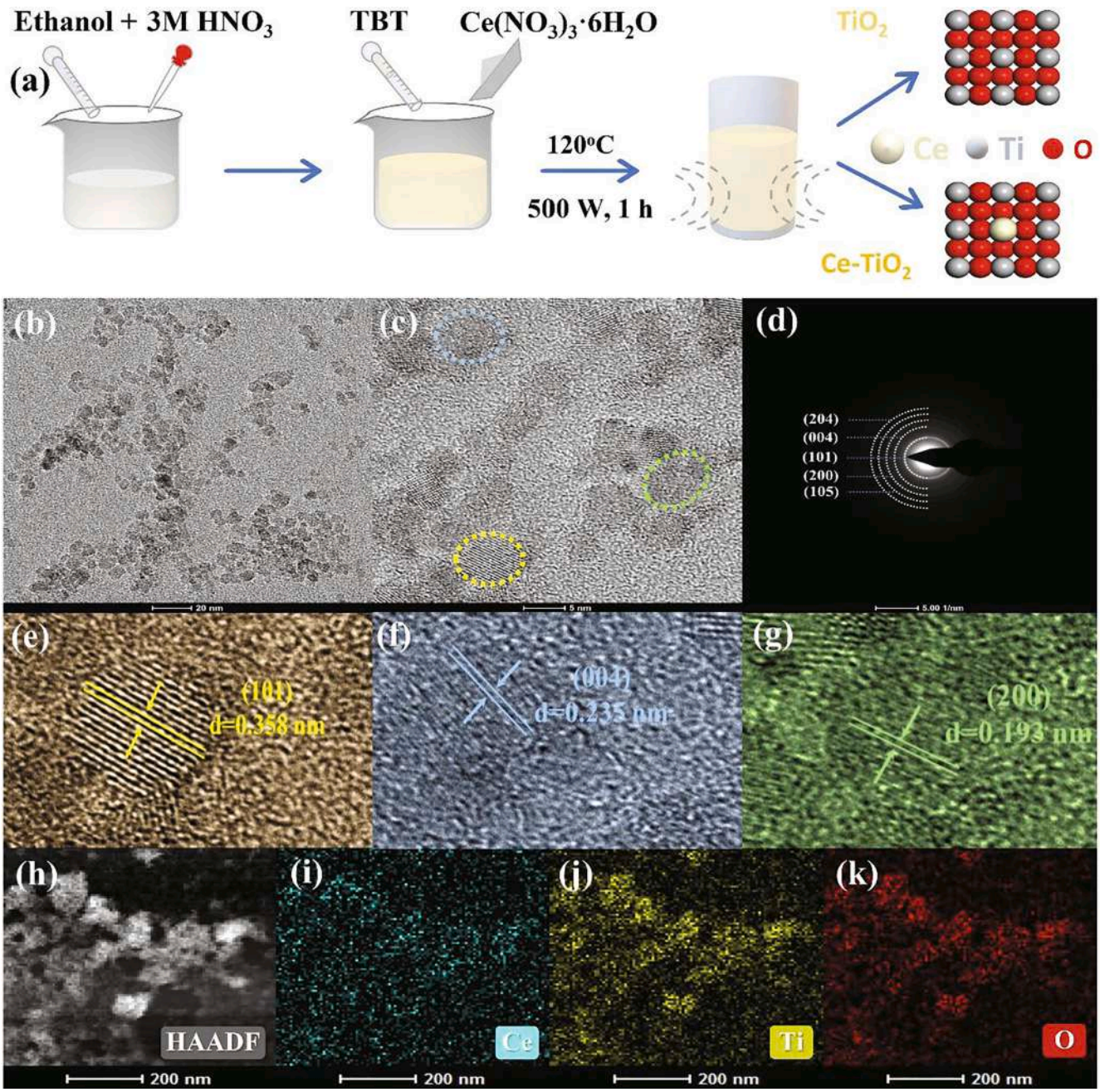

Fig. 2. (a) Schematic diagram of the synthesis procedure of pure TiO_2 and Ce-TiO_2 nanocrystals; Nanostructure details of 0.43 at% Ce-TiO_2: (b, c) HR-TEM images, (d) SAED pattern. (e-g) lattice distance of various crystal planes and (h-k) HAADF image and EDS elements mappings of 0.43 at% Ce-TiO_2.

These XRD peaks from 20° to 80° were matched well with anatase TiO_2 and there are no extra peaks, indicating that TiO_2 was synthesized successfully. Due to the Ce doping content being too low, there is no shift in all Ce-TiO_2 peaks. Additionally, the texture coefficient ($TC_{(hkl)}$) values of all samples are calculated using Eq. (2):[15].

$$TC_{(hkl)} = \frac{I_{(hkl)}/I_{0(hkl)}}{\frac{1}{n}\sum I_{(hkl)}/I_{0(hkl)}} \quad (2)$$

where $I_{(hkl)}$ is the relative peaks intensity in XRD patterns; $I_{0(hkl)}$ is the peak intensity in the standard pattern; n is the total number of peaks. The estimated TC values and the corresponding variation are presented in Table S1 and Fig. 1b. These results indicate Ce doping causes a re-orientation effect (more crystal grains are oriented at that plane if TC value is greater than 1). The TC values of (0 0 4) and (2 0 0) of 0.43 at% Ce doping are the highest, while TC values of other facets are decreased below 1. It indicates that (2 0 0) and (0 0 4) obtain preferential growth and are increasingly exposed on the surface of the Ce-TiO_2 [16]. Additionally, the surface energies sequence of crystalline anatase TiO_2 is: (1 0 1) < (1 0 0) < (0 0 1) [17]. Therefore, the introduction of Ce improves the chemical activity of sensing materials surface, resulting from the exposed facets of (0 0 4) and (2 0 0) with higher surface energies.

Fig. 2a illustrates the synthesis procedures of the pure TiO_2 and Ce-TiO_2 nanocrystals. The precipitates were synthesized under microwave dielectric heating which provided a uniform nucleation and growth environment [18]. The microstructure of all samples was observed via TEM. As shown in Fig. S3, pure TiO_2 and Ce-TiO_2 presented uniformly distributed small-size nanocrystals, and there is no obvious aggregation. The mean diameter of nanocrystals are 6.11 nm, 6.77 nm, 4.59 nm, and 5.23 nm, respectively. The smaller size will be beneficial to the sensing

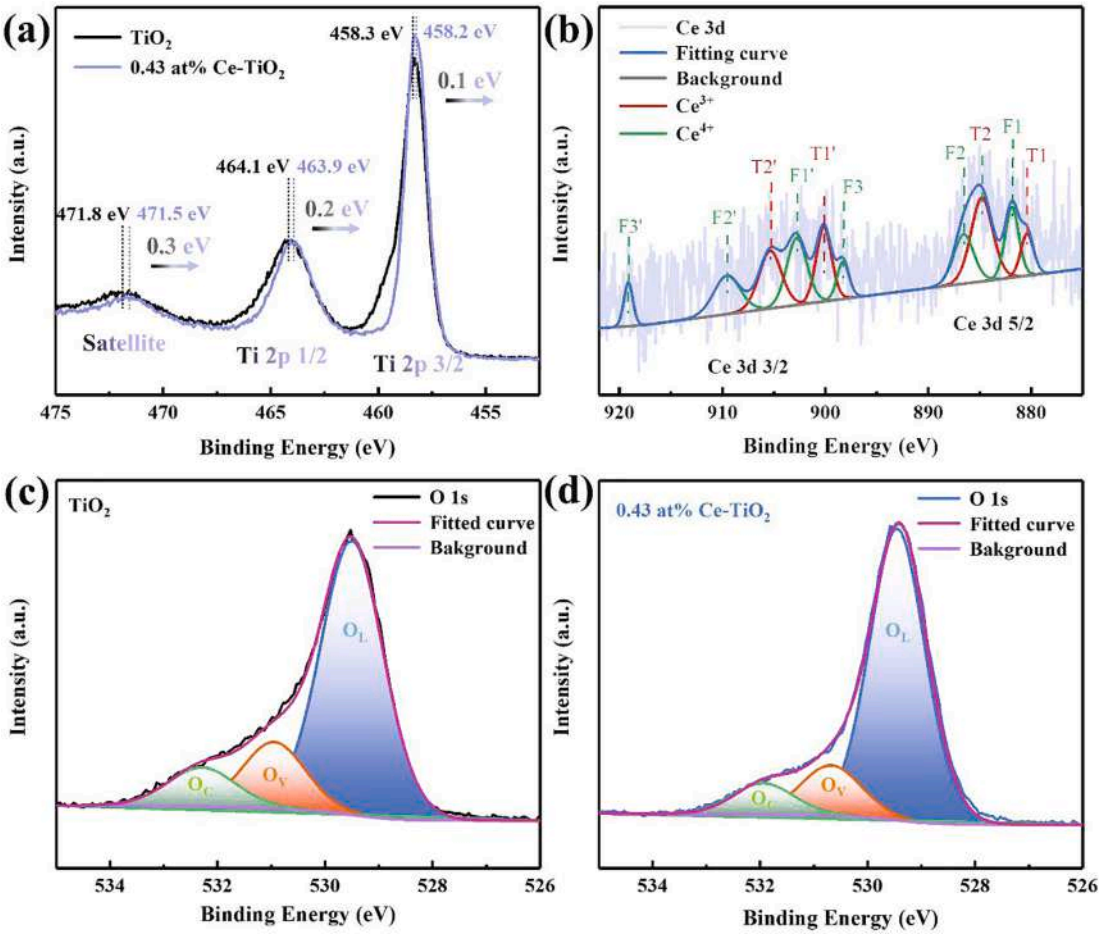

Fig. 3. Elements chemical states of pure TiO_2 and 0.43 at% Ce-TiO_2 determined via XPS: (a) Ti 2p, (b) Ce 3d, (c) O 1 s of TiO_2 and (d) O 1 s of 0.43 at% Ce-TiO_2.

properties. The nanostructure of 0.43 at% Ce-TiO_2 was further confirmed through HRTEM images. Fig. 2b and c show a similar particles distribution with TEM results. The SAED pattern in Fig. 2d shows clear spotlights spread around concentric rings, which are well-matched with crystal planes of anatase TiO_2, verifying the good crystal quality of as-synthesized 0.43 at% Ce-TiO_2 nanocrystals. Fig. 2e-g are the HRTEM images for the selected region in Fig. 2c. The crystal interplanar spacing of 0.358 nm, 0.235 nm and 0.193 nm are corresponding to (1 0 1), (0 0 4) and (2 0 0) planes of 0.43 at % Ce-TiO_2 nanocrystals, respectively. Furthermore, the uniform elements distribution of Ti and O in 0.43 at% Ce-TiO_2 was identified by energy dispersive spectroscopy (EDS) mappings (Fig. 2h- k). And Ce element was also uniformly distributed in the sample, as evidenced in Fig. 2i. Additionally, in Fig. S4, the crystal planes of (2 0 0), (0 0 4) and (1 0 1) are exposed in the two randomly selected regions. It is obvious that the (2 0 0) and (0 0 4) planes are preferred exposed on the surface, which is consistent with the XRD analysis.

The surface chemical states of pure TiO_2 and 0.43 at% Ce-TiO_2 nanocrystals were characterized via XPS. Fig. S5 shows the full survey spectrum, revealing that Ti and O elements existed in both obtained powders, and Ce ions existed in 0.43 at% Ce-TiO_2 nanocrystals. Fig. 3a shows the high-resolution Ti 2p spectrum of two samples. The peaks at around 458 eV, 464 eV and 471 eV can be attributed to representative spin–orbit split states of Ti 2p3/2, Ti 2p1/2 and the satellite,

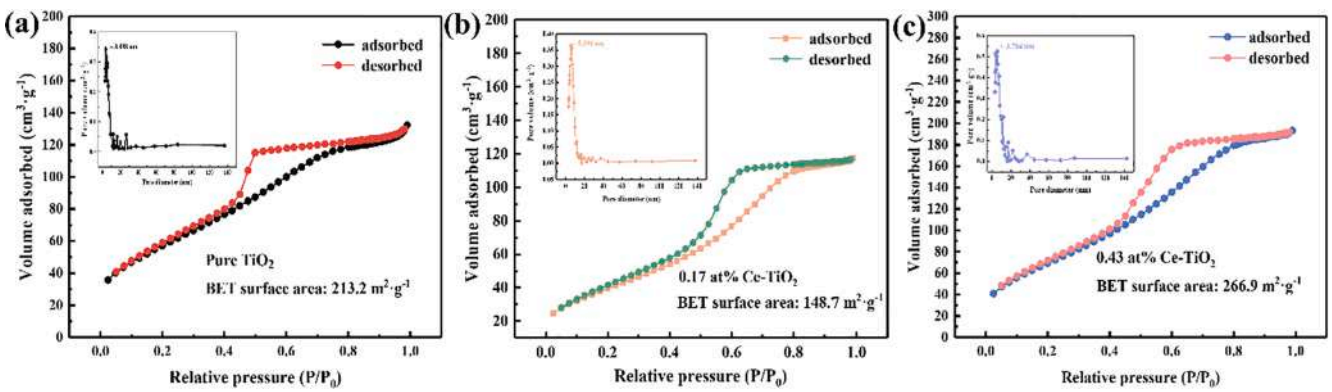

Fig. 4. N_2 adsorption–desorption isotherms and pore size distribution of (a) TiO_2, (b) 0.17 at% Ce-TiO_2 nanocrystals, and (c) 0.43 at% Ce-TiO_2 nanocrystals.

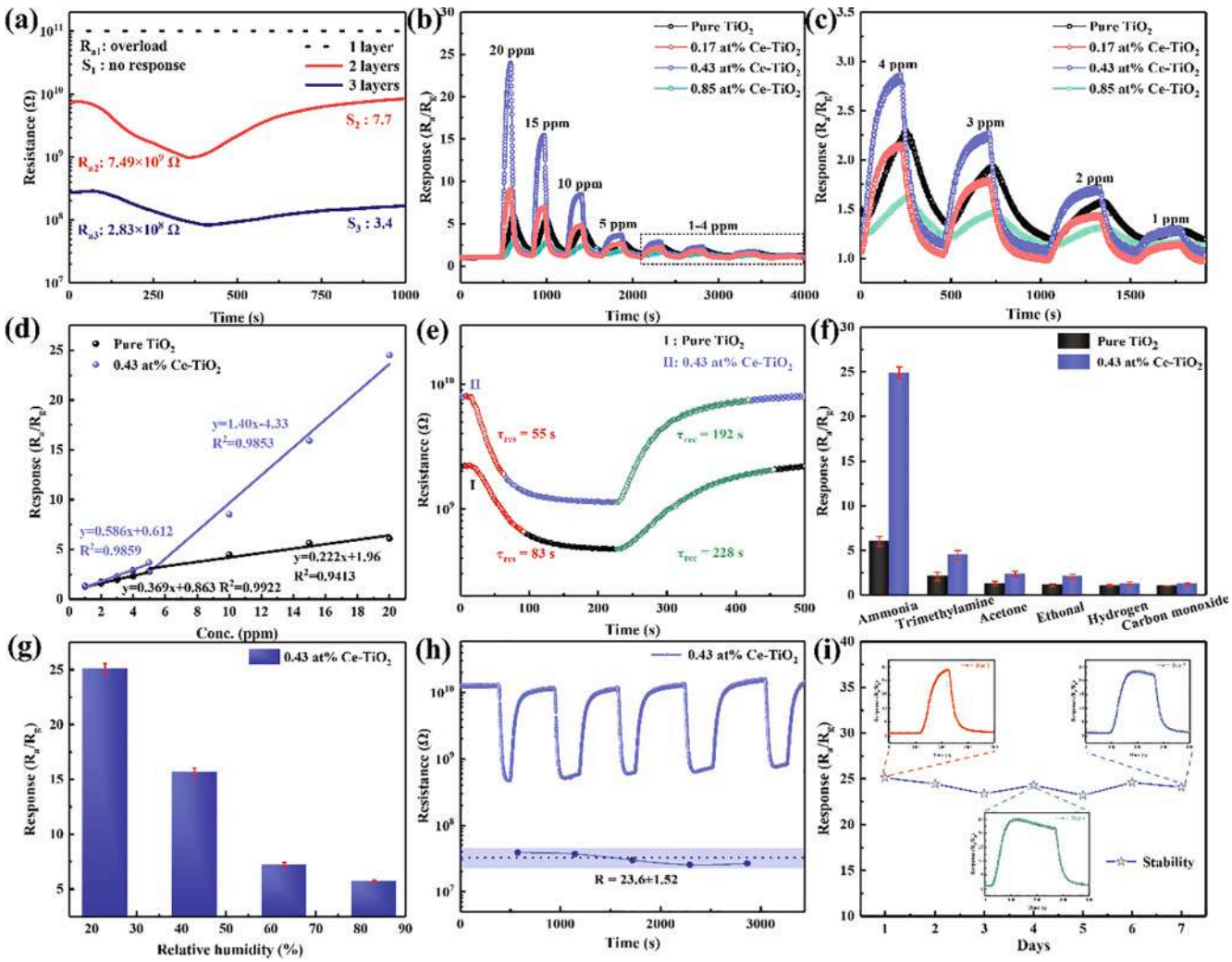

Fig. 5. (a) the variation of baseline resistance and response values versus the thickness of gas sensing layer. (b) Dynamic response/recovery curves of three samples to 1–20 ppm NH_3 at room temperature. (c) responses values to 1–20 ppm NH_3 at room temperature. (d) relationship of responses values versus NH_3 concentration. (e) responses /recovery time of 0.43 at% Ce-TiO_2 to 10 ppm NH_3 at room temperature. (f) Selectivity to 20 ppm NH_3 and various gases of 0.43 at% Ce-TiO_2 at RT. (g) the variation of response values and baseline resistance versus relative humidity. (h) Response to 20 ppm NH_3 of 0.43 at% Ce-TiO_2 in 5 cycles. (i) Response stable characteristics of 0.43 at% Ce-TiO_2 sensor to 20 ppm NH_3 in one week.

respectively [19]. The shift to the lower binding energy of Ti 2p of 0.43 at% Ce-TiO_2 sample indicates Ce ions was doped into the TiO_2 lattice [20]. As shown in Fig. 3b, the XPS spectra of Ce 3d can be indexed to several peaks labeled as T1′, F1′, T2′, F2′ and F3′ located at 900.1, 902.8, 905.2, 909.5 and 919.0 eV, and T0, T1, F1, T2, F2 and F3 located at 880.4, 881.7, 884.8, 886.5 and 898.2 eV, respectively [21]. The peaks F1, F2, F3, F1′, F2′, and F3′ are ascribed to Ce^{4+}, and the T1, T2, T1′ and T2′ are related to Ce^{3+} [12]. Fig. 3c presents the O 1 s spectra of pure TiO_2 with three peaks: lattice oxygen (O_L) at around 529.5 eV, oxygen vacancy (O_V) at around 531.0 eV, and chemisorbed oxygen (O_C) at 532.3 eV [22]. As for 0.43 at% Ce-TiO_2 (Fig. 3d), the corresponding peaks shift to the lower binding energy of 529.4, 530.6, and 531.9 eV. The induced oxygen defects will be conducive to obtain the superior gas-sensing performance.

The BET specific surface areas of pure TiO_2, 0.17 at% Ce-TiO_2 and 0.43 at% Ce-TiO_2 samples were tested. The isotherm plots of TiO_2, 0.17 at% Ce-TiO_2 and 0.43 at% Ce-TiO_2 nanocrystals are displayed in Fig. 4. The calculated BET specific surface areas of TiO_2, 0.17 at% Ce-TiO_2 and 0.43 at% Ce-TiO_2 nanocrystals were 213.2, 148.7 and 266.9 $m^2 \cdot g^{-1}$, respectively. As shown in Table S3, the average pore sizes of pure TiO_2, 0.17 at% Ce-TiO_2 and 0.43 at% Ce-TiO_2 were 3.498, 5.490 and 3.704 nm, respectively. Moreover, 0.43 at% Ce-TiO_2 also present a large total pore volume of 0.299 $cm^3 \cdot g^{-1}$, while that of pure TiO_2 and 0.17 at% Ce-TiO_2 was 0.204 and 0.181 $cm^3 \cdot g^{-1}$, respectively. The specific surface area is related to crystal size ($S = 6 / D * \rho$, where S is the specific surface area, D is the crystal size, and ρ is the density of the crystal). Hence, the variation of specific surface area is corresponding to the crystal size calculated from TEM images. Hence, the modified surface characteristics of 0.43 at% Ce-TiO_2 will boost the adsorption and transportation of gas molecules, which is in favor of attaining superior sensing properties [23].

3.2. Gas sensing properties

Pure TiO_2 and Ce-TiO_2 nanocrystals gas sensors were measured under room temperature. First, the effect of operating temperature of 0.43 at% Ce-TiO_2 on gas sensors was firstly investigated by exposing to 10 ppm NH_3. Fig. S6 shows the response values decreased when the temperature was 50–100 °C, suggesting room temperature is the optimum choice. The regulation of the metal oxides film thickness also plays a role on the gas sensor [24]. Hence, the influence of sensing layer thickness on the response to 10 ppm NH_3 was evaluated. Taking 0.43 at % Ce-TiO_2 gas sensor as an example, we prepared a series of sensing films via coated for 1, 2 and 3 times (Fig. S7). The different response/

recovery plots in Fig. 5a point that the thickness affects the baseline resistance in air and the response. The thickness of one layer is too thin to acquis the overload resistance. The response values and resistance decrease as the layer thickness increases, which is consistent with the reported literature [13]. As a result, the 2-times coated sensing layer is currently the optimal thickness for our study.

Fig. 5b and 5c display the transient response/recovery behaviors of all gas sensors at room temperature. The gas sensors show fine response towards 1–20 ppm NH_3, which may benefit from the small particle size effect [25,26]. Notably, the response values of 0.43 at% Ce-TiO_2 sensor are significantly higher than that of pure TiO_2, 0.17 at% Ce-TiO_2 and 0.85 at% Ce-TiO_2. The response values of 0.43 at% Ce-TiO_2 to 1–20 ppm NH_3 are from 1.3 to 23.99, while pure TiO_2 to 20 ppm NH_3 is only 6.1. In Fig. 5d, the fitted curves show 0.43 at% Ce-TiO_2 gas sensor possessed a linear relationship (Slope: 0.586 and 1.400; $R^2 = 0.9859$ and 0.9853) with NH_3 in both low-concentration (1–5 ppm) and high-concentration range (5–20 ppm), which is better than that of pure TiO_2 (Slope: 0.369 and 0.222; $R^2 = 0.9922$ and 0.9413). The results indicate that 0.43 at% Ce-TiO_2 nanocrystals sensor shows a higher sensitivity for NH_3 gas detection and fine linearity, which favor quantitative analysis [27]. Furthermore, the response/recovery speed was also evaluated at the same conditions. The 0.43 at% Ce-TiO_2 gas sensor exhibited an improved response/recovery speed (55 s/192 s) towards 10 ppm NH_3, while that of pure TiO_2 was 83 s and 228 s, respectively.

The theoretical limit of detection (LOD) of 0.43 at% Ce-TiO_2 was calculated through the corresponding definition equation ($LOD = 3\ RMS_{noise}/k$) [9]. Based on 100 baseline resistance points of 0.43 at% Ce-TiO_2 from Fig. 5d. The RMS_{noise} of 0.43 at% Ce-TiO_2 is calculated to be 0.00075, k is the slopes of the linear fitting curves in the range of 1–5 ppm, which is 0.586 for 0.43 at% Ce-TiO_2. Hence, the LOD value of 0.43 at% Ce-TiO_2 sensor is estimated to be 140 ppb, which can meet the practical application. The LOD of pure TiO_2 (290 ppb) was also calculated through the same equation, which is worse than the 0.43 at% Ce-TiO_2 sensor.

Selectivity as a key role in the practical application was also be evaluated [28]. In Fig. 5f, 0.43 at% Ce-TiO_2 gas sensor was investigated using five interference gases including trimethylamine, acetone, ethanol, hydrogen, and carbon monoxide of 20 ppm at room temperature. The 0.43 at% Ce-TiO_2 nanocrystals shows the highest response of 23.99 towards NH_3, while the significantly lower response to all interference gases or vapors. To further evaluate the selectivity, the gas response ratios ($R = S_{ammonia}/S_{interference\ gas}$) was calculated. As shown in Table S2, the sensor based on 0.43 at% Ce-TiO_2 shows the significantly higher R values, indicating 0.43 at% Ce-TiO_2 presents enhanced selectivity to interference gases. Additionally, the selectivity comparisons also point that the Ce doping improves the selectivity toward NH_3 against interference gases/vapors.

The variation of relative humidity may affect the sensor performance, especially working at room temperature [4,29]. Therefore, the humidity effect on the base resistance and response of 0.43 at% Ce-TiO_2 was tested in the range of 23–83 RH%. Fig. S8 presents that the base resistance was affected by the humidity change, the base resistance decreased from $7.32 \times 10^9\ \Omega$ to $5.72 \times 10^8\ \Omega$. Fig. 5g shows the response values to 20 ppm NH_3 at various relative humidity. The sensor responses at different RH (23, 43, 63, and 83%) were 23.99, 15.7, 7.2 and 5.7, respectively. The response values decreased with increased relative humidity, which is attributed to the competed adsorption of H_2O molecules, limiting the available adsorption of oxygen and NH_3 molecules [30,31]. Therefore, the fewer adsorbed NH_3 molecules, the lower response in higher humidity.

Repeatability and operating stability also play the key roles on gas sensors. We tested the response to 20 ppm NH_3 in five continuous cycles at room temperature. Fig. 5(h) shows the response values maintain around 23.6. Fig. 5i showed the stable characteristics of 0.43 at% Ce-TiO_2 gas sensor to 20 ppm NH_3 in one week. The stable response values for 7 days indicate that 0.43 at% Ce-TiO_2 nanocrystals gas sensor attained good stability at room temperature.

Table 1
Ammonia sensing properties of metal oxides-based semiconductor sensors.

Materials	Working Condition	Conc.	Response	τ_{res}/τ_{rec}	Limit of detection (ppb)	Refs.
TiO_2	250 °C	300 ppm	2.11[a]	–	–	[32]
N-TiO_2	20 °C	3 ppm	1.21[b]	70 s/ 300 s	1000	[33]
Pd-TiO_2	500 °C	80 ppm	1.75 [a]	100 s/ 280 s	–	[34]
TiO_2/ $Ti_3C_2T_x$	25 °C	10 ppm	1.03[b]	33 s/ 277 s	500	[35]
Pt-WO_3	125 °C	200 ppm	13.61[a]	43 s/ 272 s	–	[36]
Co_3O_4	25 °C	20 ppm	2.83[b]	220 s/ 830 s	1000	[37]
CeO_2	25 °C	100 ppm	10.1 [a]	–	500	[38]
CuPc-ZnO	27 °C	100 ppm	15.8 [a]	–	800	[39]
0.43 at% Ce-TiO_2	25 °C	20 ppm	23.99 [a]	25 s/ 272 s	140	This work

[a] $S = R_a/R_g$, [b] $S = R_g/R_a$.

As summarized in Table 1, 0.43 at% Ce-TiO_2 nanocrystals-based gas sensor shows superior room temperature NH_3 sensing properties than other TiO_2 based gas sensors. Additionally, compared with other reported semiconductors gas sensors, 0.43 at% Ce-TiO_2 nanocrystals gas sensor still exhibits the advanced NH_3 sensing properties working at room temperature. Hence, it will be a competitive room temperature NH_3 sensor in practical application.

3.3. Gas sensing mechanism

The electrical signal change resulting from the reaction between the surface adsorbed oxygen and target gases molecules was used to clarify the gas sensing mechanism [40,41]. Fig. 6 displays the schematic sensing procedure and mechanism of pure TiO_2 and Ce-TiO_2 based NH_3 sensors. When the gas sensors are exposed to air at room temperature, free electrons transfer to the surface from the conduction band and generate adsorbed oxygen ions, O_2^- (ads) (Eq. 3 and 4). Meanwhile, the energy band will bend up and the electron depletion layer will be formed at the interface, resulting in the formation of Schottky barrier and high resistance of the gas sensors. Once the gas sensors are exposed to target gases, the chemical reaction between oxygen ions with reducing NH_3 molecules (Eq. 5 and 6) will release electrons and lower the height of Schottky barriers, thinner the electron depletion layer, and there will display a low resistance.

$$O_{2\ (gas)} \rightarrow O_{2\ (ads)} \quad (3)$$

$$O_{2\ (ads)} + e^- \rightarrow O_{2\ (ads)}^- \quad (4)$$

$$NH_{3\ (gas)} \leftrightarrow NH_{3\ (ads)} \quad (5)$$

$$4NH_{3\ (ads)} + 3O_{2\ (ads)}^- \rightarrow 2\ N_2 + 6H_2O + 3e^- \quad (6)$$

Based on the proposed NH_3 sensing mechanism, the change of carrier concentration is a key factor in gas sensing procedures. The gas response (S) can be defined as Eq. (7) [21,42]:

$$S = \frac{R_a}{R_g} = \frac{c_g}{c_a} = \frac{\Delta c}{c_a} + 1 \quad (7)$$

where c_g and c_a represent the electron concentration in target gas and air, $\Delta c = c_g - c_a$ is the corresponding variation. The lower the electrons concentration in air and the larger electrons concentration variation is,

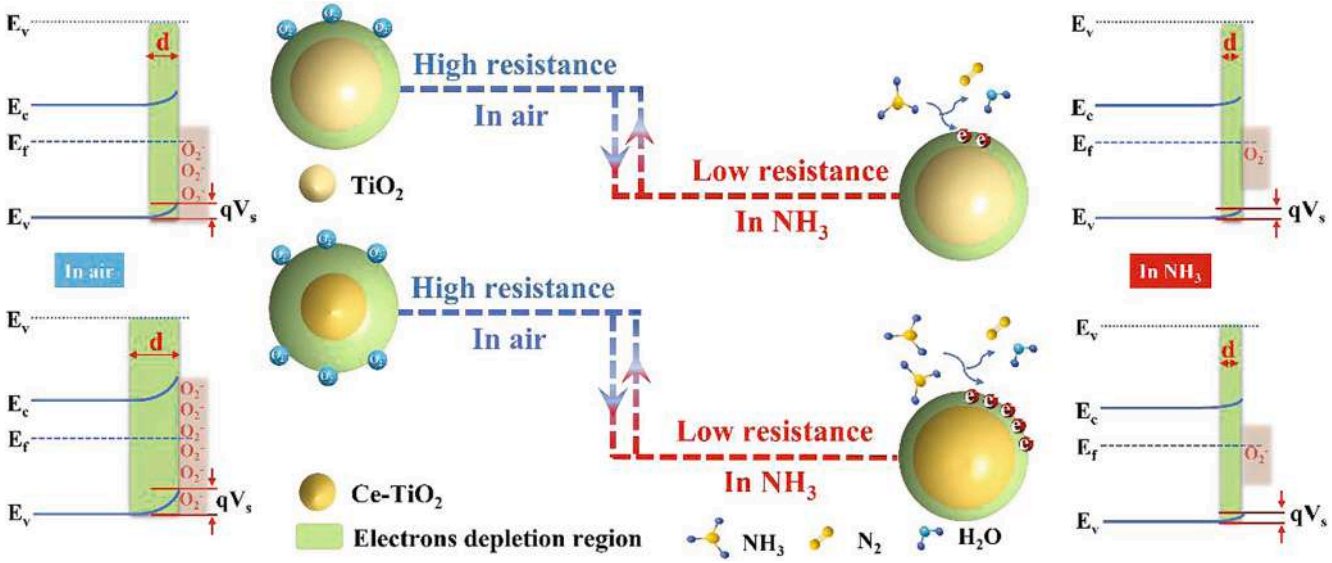

Fig. 6. Schematic illustration of the gas-sensing mechanism of pure TiO_2 and Ce-TiO_2 nanocrystals-based gas sensor for detecting NH_3 at room temperature.

Table 2
Comparison of XPS data for O1 s peak analysis on pure TiO_2 and 0.43 at% Ce-TiO_2 nanostructures.

Samples	Oxygen species	Binding energy (eV)	Percentage
Pure TiO_2	O_L	529.5	84.34 %
	O_V	531.0	9.31 %
	O_C	532.3	6.35 %
0.43 at% Ce-TiO_2	O_L	529.4	75.69 %
	O_V	530.6	14.55 %
	O_C	531.9	9.76 %

the higher response towards the reducing gas can be.

Hence, the enhanced sensing mechanism could be explained by the following three aspects. First, the preferentially grown high-energy facets of Ce-TiO_2 nanocrystals exhibit improved surface activity, attaining a higher activity for the oxidation of NH_3 and accelerating the reaction between NH_3 and adsorbed oxygen ions (Eq. 6) [43]. Second, 0.43 at% Ce-TiO_2 possessed a larger specific surface area of 266.9 $m^2 \cdot g^{-1}$ than that of pure TiO_2, which can provide abundant adsorption sites and improve the efficiency of the interface redox reaction compared with pure TiO_2. As shown in Table S3, the increased total pore volume and pore diameter of 0.43 at% Ce-TiO_2 also favor the diffusion of NH_3, leading to a faster response [44]. Third, the O1s spectra of pure TiO_2 and Ce-TiO_2 nanocrystals (Fig. 3c and 3d, Table 2) proved that 0.43 at% Ce-TiO_2 possesses more total oxygen species (O_v and O_c) in the crystal. Fig. S9 also presents the room temperature EPR spectra. The signal of 0.43 at% Ce-TiO_2 at $g = 2.003$ is significantly enhanced, revealing the increased oxygen defects in 0.43 at% Ce- TiO_2 [45]. Fig. 7c illustrates the generation of oxygen vacancies in the TiO_2 lattice. The Ce

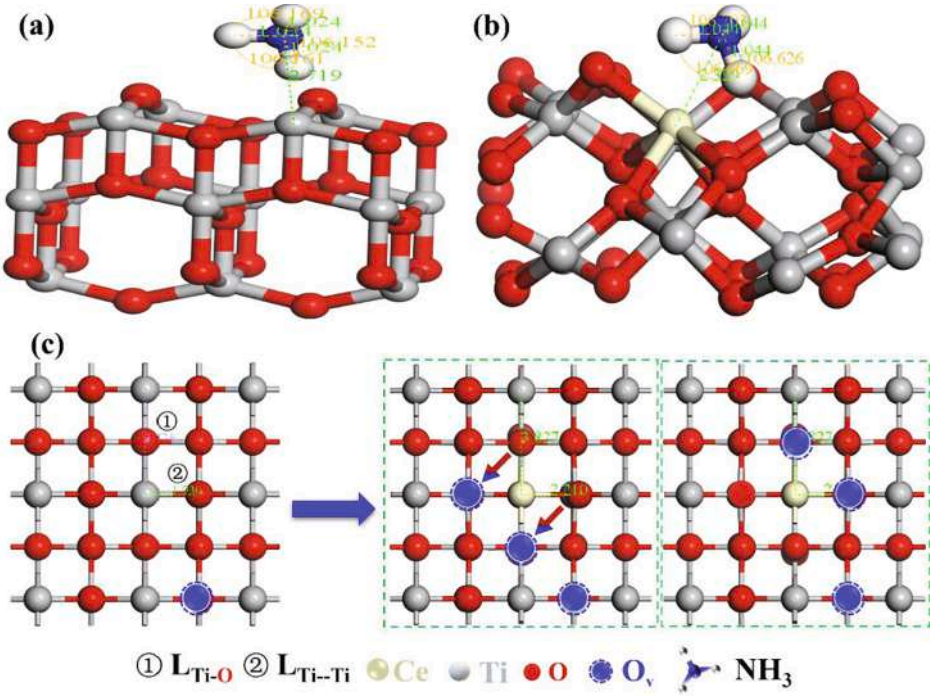

Fig. 7. Geometry structure for NH_3 adsorption systems of (a) pure TiO_2 and (b) Ce-TiO_2, (c) illustration of the generation of more oxygen vacancies in TiO_2 lattice.

Table 3
The special parameters of (0 0 1) TiO_2 and Ce-TiO_2 adsorption systems.

Samples	Bond length (Å)	Bond angle (°)	Distance (Å)	E_{ad} (eV)
	N–H	H-N–H		
Pure TiO_2	1.024	106.161	2.719	−0.59
	1.024	106.152		
	1.024	106.169		
0.43 at% Ce-TiO_2	1.044	106.703	2.329	−2.12
	1.044	106.626		
	1.044	106.669		

ions with higher metal activity than Ti ions increase the content of oxygen vacancies in the TiO_2 lattice through capturing oxygen ions from the TiO_2 lattice [46]. The Ce-TiO_2 with increased oxygen vacancy (O_V) content can enhance donor effect, leading to more surface adsorbed oxygen species and the thicker depletion layer as well as a higher Schottky barrier [47,48].

As a result of the above three aspects, there will be more surface adsorbed oxygen ions, and the carrier concentration in air (c_a) of 0.43 at % Ce-TiO_2 will be significantly lower. The efficient interface redox reaction will make the carrier concentration variation (Δc) larger. In Fig. S10, 0.43 at% Ce-TiO_2 show a higher baseline resistance (R_a) and a larger resistance variation (Δ R). The experimental details further confirm the proposed mechanism. Hence, the enhanced sensing properties could be obtained for 0.43 at% Ce-TiO_2 sensor.

To theoretically illustrate the enhanced mechanism of the Ce doped TiO_2 based gas sensing material, the adsorption behaviors were studied using DFT calculations. The adsorption models of NH_3 on the (0 0 1) plane of TiO_2 and Ce-TiO_2 were selected to calculate the adsorption energy. As shown in Fig. 7 and Table 3, the corresponding adsorption energies of NH_3 on the cleaved surface are −0.59 eV and −2.12 eV, respectively. The lower NH_3 adsorption energy on Ce-TiO_2 is also advantageous to its superior sensing performance [49]. The bond changes of NH_3 molecules are also studied by combing the geometric configuration after adsorption. The N–H bond in the Ce-TiO_2 adsorption system is elongated obviously, the distance between the NH_3 molecules and the surface becomes shorter, indicating that the Ce incorporation significantly improved the NH_3 adsorption and electron transfer [50].

3.4. Fish spoilage detection

The practical application potential of the as-fabricated gas sensors should be evaluated. During the spoilage process, fish's fatty acids and amino acids will be decomposed through microbial degradation. Herein, the practicability of 0.43 at% Ce-TiO_2 nanocrystals-based gas sensor was studied using a homemade testing system for detecting the released volatile gases from fish (tail section of Pangasius). As shown in Fig. 8a, the NH_3 released from 25 g fish during the storage at room temperature can be detected. Fig. 8b-f show the response/recover transient curves of 0.43 at% Ce-TiO_2 gas sensor at different storage periods. The response values increased from 1.66 to 7.98 as the storage time became longer. As for the freshness assessment, 5 ppm NH_3 was recommended to indicate the beginning of fish spoilage, which can be changed according to different parts of fish or storage conditions [3,51]. In Fig. 8g, 0.43 at% Ce-TiO_2 gas sensor shows the increased response values with the

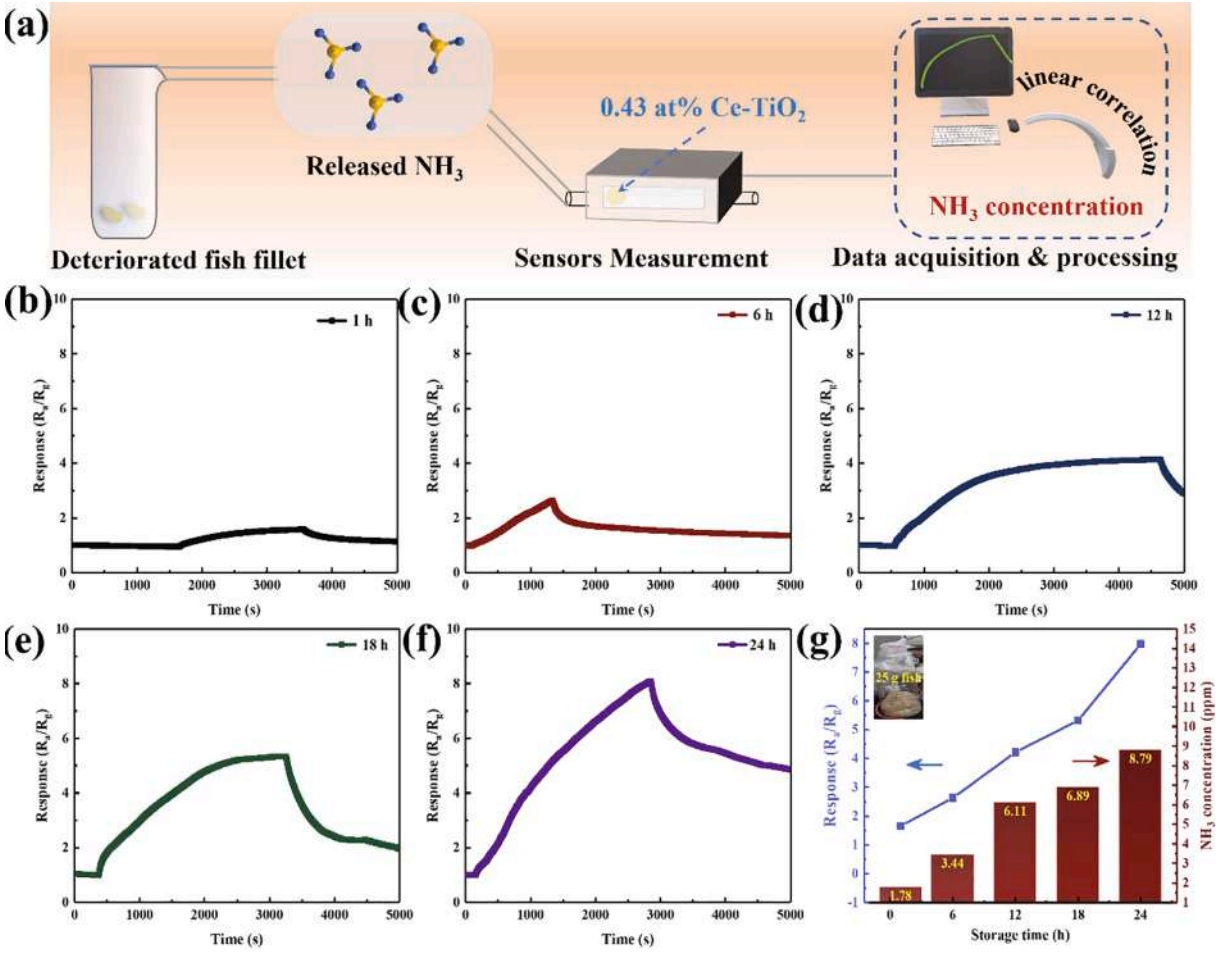

Fig. 8. (a) Schematic diagram of the fish spoilage assessment system, (b-f) Responses of the 0.43 at% Ce-TiO_2 gas sensor towards the released gases from 25 g pangasius fillet during different stages (1, 6, 12, 18, 24 h). (g) Response values of 0.43 at% Ce-TiO_2 gas sensor and the corresponding released NH_3 concentration.

increase in NH_3 concentration. The NH_3 concentration does not exceed 5 ppm during 6 h, indicating the fish fillet still maintains acceptable freshness. However, during 12–24 h, the released NH_3 concentration rapidly exceeds 6 ppm, indicating the spoilage occurs sharply under a long-term microbe decomposition [52]. Hence, the results further confirmed the promising potential of 0.43 at% Ce-TiO_2 gas sensor for NH_3 detection.

4. Conclusion

In this work, we synthesized anatase TiO_2 and Ce-TiO_2 nanocrystals-based NH_3 gas sensors using simple microwave-assisted solvothermal synthesis. The synergetic strategy of ultra-small size nanostructure and low atomic fractions Ce doping was used for fabricating high-performance gas sensors working at room temperature. The 0.43 at% Ce-TiO_2 showed the highest response to 1–20 ppm NH_3 at room temperature and improved response/recover speed, detection limit (140 ppb), selectivity, and operating stability. The enhanced sensing mechanism of Ce-TiO_2 was explained by combining the experimental results and DFT simulations. Finally, the as-fabricated gas sensor was applied in detecting volatile gas from fish spoilage to confirm the practical application potential.

Declaration of Competing Interest

The authors declare that they have no known competing financial interests or personal relationships that could have appeared to influence the work reported in this paper.

Acknowledgment

This work is supported by the National Key Research and Development Program of China under Grant No. 2017YFE0115900, the Natural Science Foundation of China under Grant No. 51872254, the Outstanding Youth Foundation of Jiangsu Province of China under Grant No. BK20211548, the Postgraduate Research & Practice Innovation Program of Jiangsu Province under Grant No. KYCX21_3229 and the Excellent Doctoral Dissertation Fund of Yangzhou University (2021).

Appendix A. Supplementary data

Supplementary data to this article can be found online at https://doi.org/10.1016/j.cej.2022.136449.

References

[1] D. Zhang, Z. Yang, P. Li, M. Pang, Q. Xue, Flexible self-powered high-performance ammonia sensor based on Au-decorated $MoSe_2$ nanoflowers driven by single layer MoS_2-flake piezoelectric nanogenerator, NANO Energy. 65 (2019), 103974, https://doi.org/10.1016/j.nanoen.2019.103974.

[2] L.-Y. Chang, M.-Y. Chuang, H.-W. Zan, H.-F. Meng, C.-J. Lu, P.-H. Yeh, J.-N. Chen, One-minute fish freshness evaluation by testing the volatile amine gas with an ultrasensitive porous-electrode-capped organic gas sensor system, ACS Sens. 2 (2017) 531–539, https://doi.org/10.1021/acssensors.6b00829.

[3] Z. Yuan, M. Bariya, H.M. Fahad, J. Wu, R. Han, N. Gupta, A. Javey, Trace-level, multi-gas detection for food quality assessment based on decorated silicon transistor arrays, Adv. Mater. 32 (2020) 1908385, https://doi.org/10.1002/adma.201908385.

[4] D. Wang, D. Zhang, Y. Yang, Q. Mi, J. Zhang, L. Yu, Multifunctional latex/polytetrafluoroethylene-based triboelectric nanogenerator for self-powered organ-like MXene/metal–organic framework-derived CuO nanohybrid ammonia Sensor, ACS Nano. 15 (2021) 2911–2919, https://doi.org/10.1021/acsnano.0c09015.

[5] K. Wu, J. Li, C. Zhang, Zinc ferrite based gas sensors: A review, Ceram. Int. 45 (2019) 11143–11157, https://doi.org/10.1016/j.ceramint.2019.03.086.

[6] D. Wang, D. Zhang, J. Guo, Y. Hu, Y. Yang, T. Sun, H. Zhang, X. Liu, Multifunctional poly(vinyl alcohol)/Ag nanofibers-based triboelectric nanogenerator for self-powered MXene/tungsten oxide nanohybrid NO_2 gas sensor, NANO Energy. 89 (2021), 106410, https://doi.org/10.1016/j.nanoen.2021.106410.

[7] K. Wu, C. Zhang, Facile synthesis and ppb-level H_2S sensing performance of hierarchical CuO microflowers assembled with nano-spindles, J. Mater. Sci. Mater. Electron. 31 (2020) 7937–7945, https://doi.org/10.1007/s10854-020-03332-8.

[8] D. Wang, D. Zhang, Q. Mi, A high-performance room temperature benzene gas sensor based on $CoTiO_3$ covered TiO_2 nanospheres decorated with Pd nanoparticles, Sens. Actuators B Chem. 350 (2022), 130830, https://doi.org/10.1016/j.snb.2021.130830.

[9] K. Wu, Y. Lu, Y. Liu, Y. Liu, M. Shen, M. Debliquy, C. Zhang, Synthesis and acetone sensing properties of copper (Cu^{2+}) substituted zinc ferrite hollow micro-nanospheres, Ceram. Int. 46 (2020) 28835–28843, https://doi.org/10.1016/j.ceramint.2020.08.049.

[10] S. Zhao, Y. Shen, A. Li, Y. Chen, S. Gao, W. Liu, D. Wei, Effects of rare earth elements doping on gas sensing properties of ZnO nanowires, Ceram. Int. 47 (2021) 24218–24226, https://doi.org/10.1016/j.ceramint.2021.05.133.

[11] Z.-H. Ma, R.-T. Yu, J.-M. Song, Facile synthesis of Pr-doped In_2O_3 nanoparticles and their high gas sensing performance for ethanol, Sens. Actuators B Chem. 305 (2020), 127377, https://doi.org/10.1016/j.snb.2019.127377.

[12] X. Wang, T. Wang, G. Si, Y. Li, S. Zhang, X. Deng, X. Xu, Oxygen vacancy defects engineering on Ce-doped α-Fe_2O_3 gas sensor for reducing gases, Sens. Actuators B Chem. 302 (2020), 127165, https://doi.org/10.1016/j.snb.2019.127165.

[13] X. Geng, S. Li, L. Mawella-Vithanage, T. Ma, M. Kilani, B. Wang, L. Ma, C.C. Hewa-Rahinduwage, A. Shafikova, E. Nikolla, G. Mao, S.L. Brock, L. Zhang, L. Luo, Atomically dispersed Pb ionic sites in PbCdSe quantum dot gels enhance room-temperature NO_2 sensing, Nat. Commun. 12 (2021) 4895, https://doi.org/10.1038/s41467-021-25192-4.

[14] C.C. Hewa-Rahinduwage, X. Geng, K.L. Silva, X. Niu, L. Zhang, S.L. Brock, L. Luo, Reversible electrochemical gelation of metal chalcogenide quantum dots, J. Am. Chem. Soc. 142 (2020) 12207–12215, https://doi.org/10.1021/jacs.0c03156.

[15] Y. Zhang, C. Wang, L. Zhao, F. Liu, X. Sun, X. Hu, G. Lu, Preparation of Ce-doped SnO_2 cuboids with enhanced 2-butanone sensing performance, Sens. Actuators B Chem. 341 (2021), 130039, https://doi.org/10.1016/j.snb.2021.130039.

[16] G. Turgut, E. Sonmez, S. Aydın, R. Dilber, U. Turgut, The effect of Mo and F double doping on structural, morphological, electrical and optical properties of spray deposited SnO_2 thin films, Ceram. Int. 40 (2014) 12891–12898, https://doi.org/10.1016/j.ceramint.2014.04.148.

[17] B. Liu, Y. Huang, Y. Wen, L. Du, W. Zeng, Y. Shi, F. Zhang, G. Zhu, X. Xu, Y. Wang, Highly dispersive 001 facets-exposed nanocrystalline TiO2 on high quality graphene as a high performance photocatalyst, J. Mater. Chem. 22 (2012) 7484, https://doi.org/10.1039/c2jm16114a.

[18] Y. Li, Y.-L. Lu, K.-D. Wu, D.-Z. Zhang, M. Debliquy, C. Zhang, Microwave-assisted hydrothermal synthesis of copper oxide-based gas-sensitive nanostructures, Rare Met. 40 (6) (2021) 1477–1493.

[19] C. Li, Y. Sun, I. Djerdj, P. Voepel, C.-C. Sack, T. Weller, R. Ellinghaus, J. Sann, Y. Guo, B.M. Smarsly, H. Over, Shape-Controlled CeO_2 Nanoparticles: Stability and Activity in the Catalyzed HCl Oxidation Reaction, ACS Catal. 7 (2017) 6453–6463, https://doi.org/10.1021/acscatal.7b01618.

[20] S. Dey, S.C. Roy, Influence of Ce doping on morphology, crystallinity and photoelectrochemical charge transfer characteristics of TiO_2 nanorod arrays grown on conductive glass substrate, J. Alloys Compd. 881 (2021), 160481, https://doi.org/10.1016/j.jallcom.2021.160481.

[21] D. Wei, Z. Huang, L. Wang, X. Chuai, S. Zhang, G. Lu, Hydrothermal synthesis of Ce-doped hierarchical flower-like In_2O_3 microspheres and their excellent gas-sensing properties, Sens. Actuators B Chem. 255 (2018) 1211–1219, https://doi.org/10.1016/j.snb.2017.07.162.

[22] S. Bai, Y. Ma, X. Shu, J. Sun, Y. Feng, R. Luo, D. Li, A. Chen, Doping Metal Elements of WO_3 for Enhancement of NO_2-Sensing Performance at Room Temperature, Ind. Eng. Chem. Res. 56 (2017) 2616–2623, https://doi.org/10.1021/acs.iecr.6b03055.

[23] D. Wang, X. Pu, X. Yu, L. Bao, Y. Cheng, J. Xu, S. Han, Q. Ma, X. Wang, Controlled preparation and gas sensitive properties of two-dimensional and cubic structure $ZnSnO_3$, J. Colloid Interface Sci. 608 (2022) 1074–1085, https://doi.org/10.1016/j.jcis.2021.09.167.

[24] S. Kanaparthi, S.G. Singh, MoS_2 chemiresistive sensor array on paper patterned with toner lithography for simultaneous detection of NH_3 and H_2S Gases, ACS Sustain. Chem. Eng. 9 (2021) 14735–14743, https://doi.org/10.1021/acssuschemeng.1c04166.

[25] A. Rothschild, Y. Komem, The effect of grain size on the sensitivity of nanocrystalline metal-oxide gas sensors, J. Appl. Phys. 95 (2004) 6374–6380, https://doi.org/10.1063/1.1728314.

[26] C. Xu, J. Tamaki, N. Miura, N. Yamazoe, Grain size effects on gas sensitivity of porous SnO_2-based elements, Sens. Actuators B Chem. 3 (1991) 147–155, https://doi.org/10.1016/0925-4005(91)80207-Z.

[27] K. Wu, Y. Luo, Y. Li, C. Zhang, Synthesis and acetone sensing properties of $ZnFe_2O_4$/rGO gas sensors, Beilstein J. Nanotechnol. 10 (2019) 2516–2526, https://doi.org/10.3762/bjnano.10.242.

[28] J. Liu, M. Dai, T. Wang, P. Sun, X. Liang, G. Lu, K. Shimanoe, N. Yamazoe, Enhanced gas sensing properties of SnO_2 hollow spheres decorated with CeO_2 nanoparticles heterostructure composite materials, ACS Appl. Mater. Interfaces. 8 (2016) 6669–6677, https://doi.org/10.1021/acsami.6b00169.

[29] C. Zhang, K. Wu, H. Liao, M. Debliquy, Room temperature WO_3-Bi_2WO_6 sensors based on hierarchical microflowers for ppb-level H_2S detection, Chem. Eng. J. 430 (2022), 132813, https://doi.org/10.1016/j.cej.2021.132813.

[30] Q. Hu, Z. Wang, J. Chang, P. Wan, J. Huang, L. Feng, Design and preparation of hollow NiO sphere- polyaniline composite for NH_3 gas sensing at room temperature, Sens. Actuators B Chem. 344 (2021), 130179, https://doi.org/10.1016/j.snb.2021.130179.

[31] D. Wang, D. Zhang, P. Li, Z. Yang, Q. Mi, L. Yu, Electrospinning of flexible poly (vinyl alcohol)/MXene nanofiber-based humidity sensor self-powered by monolayer molybdenum diselenide piezoelectric nanogenerator, Nano-Micro Lett. 13 (2021) 57, https://doi.org/10.1007/s40820-020-00580-5.

[32] D. Majumder, S. Roy, Room temperature synthesis of TiO_2 nanospheres: Ammonia sensing characteristics, Mater. Today Proc. 5 (2018) 9811–9816, https://doi.org/10.1016/j.matpr.2017.10.171.
[33] Y. Zhou, Y. Wang, Y. Wang, H. Yu, R. Zhang, J. Li, Z. Zang, X. Li, MXene $Ti_3C_2T_x$-Derived nitrogen-functionalized heterophase TiO_2 homojunctions for room-temperature trace ammonia gas sensing, ACS Appl. Mater. Interfaces. 13 (47) (2021) 56485–56497.
[34] F. Pan, H. Lin, H. Zhai, Z. Miao, Y. Zhang, K. Xu, B. Guan, H. Huang, H. Zhang, Pd-doped TiO_2 film sensors prepared by premixed stagnation flames for CO and NH_3 gas sensing, Sens. Actuators B Chem. 261 (2018) 451–459, https://doi.org/10.1016/j.snb.2018.01.173.
[35] H. Tai, Z. Duan, Z. He, X. Li, J. Xu, B. Liu, Y. Jiang, Enhanced ammonia response of $Ti_3C_2T_x$ nanosheets supported by TiO_2 nanoparticles at room temperature, Sens. Actuators B Chem. 298 (2019), 126874, https://doi.org/10.1016/j.snb.2019.126874.
[36] Y. Wang, J. Liu, X. Cui, Y. Gao, J. Ma, Y. Sun, P. Sun, F. Liu, X. Liang, T. Zhang, G. Lu, NH_3 gas sensing performance enhanced by Pt-loaded on mesoporous WO_3, Sens. Actuators B Chem. 238 (2017) 473–481, https://doi.org/10.1016/j.snb.2016.07.085.
[37] Z. Li, Z. Lin, N. Wang, J. Wang, W. Liu, K. Sun, Y.Q. Fu, Z. Wang, High precision NH_3 sensing using network nano-sheet Co_3O_4 arrays based sensor at room temperature, Sens. Actuators B Chem. 235 (2016) 222–231, https://doi.org/10.1016/j.snb.2016.05.063.
[38] P. Li, B. Wang, C. Qin, C. Han, L. Sun, Y. Wang, Band-gap-tunable CeO_2 nanoparticles for room-temperature NH_3 gas sensors, Ceram. Int. 46 (2020) 19232–19240, https://doi.org/10.1016/j.ceramint.2020.04.261.
[39] J. Huang, D. Jiang, J. Zhou, J. Ye, Y. Sun, X. Li, Y. Geng, J. Wang, Y. Du, Z. Qian, Visible light-activated room temperature NH_3 sensor base on CuPc-loaded ZnO nanorods, Sens. Actuators B Chem. 327 (2021), 128911, https://doi.org/10.1016/j.snb.2020.128911.
[40] H. Bi, L.-X. Zhang, Y. Xing, P. Zhang, J.-J. Chen, J. Yin, L.-J. Bie, Morphology-controlled synthesis of CeO_2 nanocrystals and their facet-dependent gas sensing properties, Sens. Actuators B Chem. 330 (2021), 129374, https://doi.org/10.1016/j.snb.2020.129374.
[41] J. Miao, C. Chen, Y.S. Lin, Metal-oxide nanoparticles with a sopant-segregation-induced core–shell structure: Gas sensing properties, J. Phys. Chem. C. 122 (2018) 21322–21329, https://doi.org/10.1021/acs.jpcc.8b04391.
[42] H.-J. Kim, K.-I. Choi, K.-M. Kim, C.W. Na, J.-H. Lee, Highly sensitive C_2H_5OH sensors using Fe-doped NiO hollow spheres, Sens. Actuators B Chem. 171–172 (2012) 1029–1037, https://doi.org/10.1016/j.snb.2012.06.029.
[43] R. Xu, L.-X. Zhang, M.-W. Li, Y.-Y. Yin, J. Yin, M.-Y. Zhu, J.-J. Chen, Y. Wang, L.-J. Bie, Ultrathin SnO2 nanosheets with dominant high-energy 001 facets for low temperature formaldehyde gas sensor, Sens. Actuators B Chem. 289 (2019) 186–194, https://doi.org/10.1016/j.snb.2019.03.012.
[44] K.-D. Wu, J.-Y. Xu, M. Debliquy, C. Zhang, Synthesis and NH_3/TMA sensing properties of $CuFe_2O_4$ hollow microspheres at low working temperature, Rare Met. 40 (2021) 1768–1777, https://doi.org/10.1007/s12598-020-01609-9.
[45] R. Zhao, G. Wang, Y. Mao, X. Bao, Z. Wang, P. Wang, Y. Liu, Z. Zheng, Y. Dai, H. Cheng, B. Huang, Li-intercalation boosted oxygen vacancies enable efficient electrochemical nitrogen reduction on ultrathin TiO_2 nanosheets, Chem. Eng. J. 430 (2022), 133085, https://doi.org/10.1016/j.cej.2021.133085.
[46] Y. Zhang, Y. Liu, L. Zhou, D. Liu, F. Liu, F. Liu, X. Liang, X. Yan, Y. Gao, G. Lu, The role of Ce doping in enhancing sensing performance of ZnO-based gas sensor by adjusting the proportion of oxygen species, Sens. Actuators B Chem. 273 (2018) 991–998, https://doi.org/10.1016/j.snb.2018.05.167.
[47] C. Zhang, G. Liu, K. Liu, K. Wu, ZnO_{1-x} coatings deposited by atmospheric plasma spraying for room temperature ppb-level NO_2 detection, Appl. Surf. Sci. 528 (2020), 147041, https://doi.org/10.1016/j.apsusc.2020.147041.
[48] H. Yuan, S.A.A.A. Aljneibi, J. Yuan, Y. Wang, H. Liu, J. Fang, C. Tang, X. Yan, H. Cai, Y. Gu, S.J. Pennycook, J. Tao, D. Zhao, ZnO nanosheets abundant in oxygen vacancies derived from metal-organic frameworks for ppb-level gas sensing, Adv. Mater. 31 (2019) 1807161, https://doi.org/10.1002/adma.201807161.
[49] D. Zhang, J. Wu, P. Li, Y. Cao, Room-temperature SO_2 gas-sensing properties based on a metal-doped MoS_2 nanoflower: an experimental and density functional theory investigation, J. Mater. Chem. A. 5 (2017) 20666–20677, https://doi.org/10.1039/C7TA07001B.
[50] D. Zhang, W. Pan, L. Zhou, S. Yu, Room-temperature benzene sensing with Au-doped ZnO nanorods/exfoliated WSe_2 nanosheets and density functional theory simulations, ACS Appl. Mater. Interfaces. 13 (2021) 33392–33403, https://doi.org/10.1021/acsami.1c03884.
[51] Z. Ma, P. Chen, W. Cheng, K. Yan, L. Pan, Y. Shi, G. Yu, Highly sensitive, printable nanostructured conductive polymer wireless sensor for food spoilage detection, NANO Lett. 18 (2018) 4570–4575, https://doi.org/10.1021/acs.nanolett.8b01825.
[52] D. Zhang, S. Yu, X. Wang, J. Huang, W. Pan, J. Zhang, B.E. Meteku, J. Zeng, UV illumination-enhanced ultrasensitive ammonia gas sensor based on (001)TiO_2/MXene heterostructure for food spoilage detection, J. Hazard. Mater. 423 (2022), 127160, https://doi.org/10.1016/j.jhazmat.2021.127160.